

Droplet motion on chemically heterogeneous substrates with mass transfer. II. Three-dimensional dynamics

Danny Groves

School of Mathematics, Cardiff University, Cardiff, CF24 4AG, UK

Nikos Savva*

Computation-based Science and Technology Research Center, The Cyprus Institute, Nicosia 2121, Cyprus

We consider a thin droplet that spreads over a flat, horizontal and chemically heterogeneous surface. The droplet is subjected to changes in its volume through a prescribed, arbitrary spatio-temporal function, which varies slowly and vanishes along the contact line. A matched asymptotics analysis is undertaken to derive a set of evolution equations for the Fourier harmonics of nearly circular contact lines, which is applicable in the long-wave limit of the Stokes equations with slip. Numerical experiments highlight the generally excellent agreement between the long-wave model and the derived equations, demonstrating that these are able to capture many of the features which characterize the intricate interplay between substrate heterogeneities and mass transfer on droplet motion.

I. INTRODUCTION

When the size of a droplet changes as it spreads, a number of interesting effects emerge. Alongside the usual pinning, stick-slide and stick-jump modes observed in the absence of mass transfer, these also include, e.g. the constant-radius, constant-angle and the recently reported snapping modes (see, e.g. Refs. [1–6]; see also Ref. [7] and the references therein). Such effects are commonly attributed to local variations in the substrates' topographical and/or chemical features, which may temporarily trap the contact line [7, 8]. Due to the highly nonlinear and multi-scale nature of the mechanisms underpinning the dynamics of contact lines, investigations based on purely computational approaches are highly non-trivial and are currently capable of only partly resolving the lengthscales present [9–11].

Within the long-wave approximation and for weakly distorted contact lines, lower-dimensional models were derived for droplets of fixed volume that were capable of accurately capturing the evolution of contact lines in three dimensions (3D), and at a fraction of the computing cost that would have been required for simulating the full long-wave model [12]. The present study offers an extension to Ref. [12] to perform, for the first time, a matched asymptotic analysis for non-axisymmetric, 3D droplets of variable mass. It constitutes the second part of the work undertaken by the present authors which considered the same setting in two-dimensions (2D) (see Ref. [7], hereinafter referred to as Part I). As in these aforementioned studies, we pursue a combined analytical and numerical investigation on a long-wave evolution equation for the droplet thickness, which is derived by considering thin viscous droplets in the gravity-free regime with strong surface tension effects and negligible inertia [13]. Assuming that the spreading of the droplet and the rate of liquid flux is slow, analytical progress is possible in the limit of vanishingly small slip lengths with the method of matched asymptotic expansions. In this manner, the dynamics of the macro-scale where capillary forces dominate are coupled with the processes governing the micro-scale where slip effects manifest themselves, to ultimately yield a set of simpler equations that approximates the full model [14, 15].

To avoid the complications of the analysis arising in the 2D counterpart where transcendental equations need to be solved for the contact point velocities [7, 16], we assume that the liquid flux vanishes at the contact line so that explicit expressions can be derived for the contact line velocity. While this assumption is not appropriate for describing mass loss through evaporation since the evaporative flux is maximized there [17–19], we have shown in Ref. [7] that many of the interesting features observed in studies involving evaporating droplets are rather general, and characterize the dynamics captured by the present model. A key contribution of this work is that the more realistic 3D model allows us to make comparisons with experimental observations, so that features such as the stick-slip events observed by Dietrich *et al.* for evaporating droplets [3], and the constant-radius and constant-angle modes observed by Lam *et al.* for fluid pumping through a needle [2], can be explored by varying the parameters controlling the liquid flux and chemical heterogeneity.

This study is structured as follows. In Sec. II we present the model and its assumptions. Using the method of matched asymptotic expansions in Sec. III, we derive a reduced model for the motion of the contact line that consists

* Corresponding author: n.savva@cyi.ac.cy

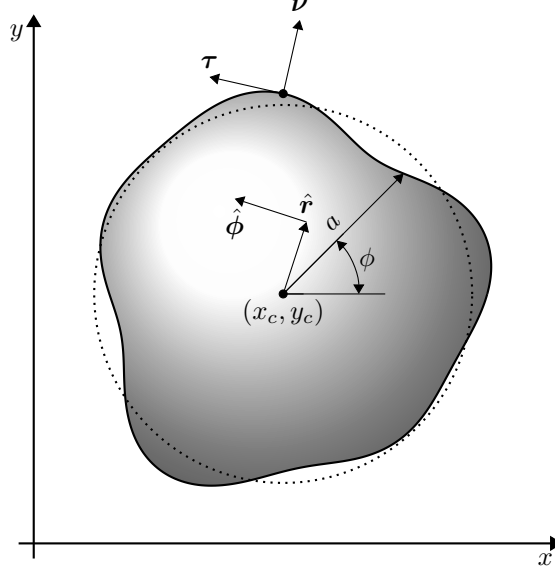


FIG. 1. A top view of the geometry highlighting the wetted region $\Omega(t)$ (in shaded gray). The contact line \mathbf{c} is described by the polar curve $a(\phi, t)$ in the coordinate system with origin at (x_c, y_c) and corresponds to a perturbation from a circle (dotted curve). The vectors $\hat{\mathbf{r}}$ and $\hat{\boldsymbol{\phi}}$ represent the unit radial and azimuthal vectors in the moving frame, respectively; $\boldsymbol{\nu}$ and $\boldsymbol{\tau}$ denote the outward unit normal and tangent vectors to the contact line \mathbf{c} , respectively.

of a set of integro-differential equations, which approximates the dynamics of the full model of Sec. II. In Sec. IV the results of the analysis are scrutinized against numerical solutions to the governing partial differential equation (PDE) to extract insights on the interplay between mass flux and surface heterogeneities, contrasting, where appropriate, the results in Part I of this study. Concluding remarks are offered in Sec. V.

II. PROBLEM FORMULATION

Consider a droplet in 3D moving on a flat, horizontal and chemically heterogeneous substrate under the action of capillary pressure and mass transfer effects. The problem formulation and assumptions closely follows Part I, so that the corresponding non-dimensional long-wave PDE which governs the evolution of the droplet thickness $h(\mathbf{x}, t)$ is given by

$$\partial_t h + \nabla \cdot [h(h^2 + \lambda^2) \nabla \nabla^2 h] = q, \quad (1a)$$

where $q(\mathbf{x}, t)$ models the mass flux, λ is the slip length and the gradient and Laplacian operators are defined in 2D. Eq. (1) is made non-dimensional by scaling the lateral scales with $L = [V/(2\pi\alpha_s)]^{1/3}$, time with $\tau = 3\mu L/(\sigma\alpha_s^3)$, and q with ρ/τ where σ is the surface tension, μ the viscosity, and V and α_s are some reference values for the volume and contact angle, respectively. The substrate is decorated with chemical heterogeneities, which are described with locally varying contact angles according to $\theta(\mathbf{x})$, as scaled with respect to α_s . Along the contact line, $\mathbf{x} = \mathbf{c}$, we have

$$h = 0, \quad |\nabla h| = \theta \quad \text{and} \quad \theta (\partial_t \mathbf{c} - \lambda^2 \nabla \nabla^2 h) \cdot \boldsymbol{\nu} = q, \quad (1b,c,d)$$

where $\boldsymbol{\nu}$ denotes the outward unit normal vector to the contact line (see Fig. 1). We note here that, just as in the 2D case [7], condition (1d) is of kinematic type and arises from a local expansion of Eq. (1a) near $\mathbf{x} = \mathbf{c}$ so that

$$\frac{d}{dt} \int_{\Omega(t)} h(\mathbf{x}, t) d\mathbf{x} = \int_{\Omega(t)} q(\mathbf{x}, t) d\mathbf{x} = \dot{v}(t), \quad (1e)$$

as well as Eqs. (1b) and (1c) simultaneously hold (see appendix for an outline of the derivation of Eq. (1d)). In Eq. (1e), $\Omega(t)$ and $v(t)$ denote, respectively, the wetted region of the substrate and the (dimensionless) droplet volume. In the present study we assume that $q \rightarrow 0$ as $\mathbf{x} \rightarrow \mathbf{c}$, so that Eq. (1d) reduces to $(\partial_t \mathbf{c} - \lambda^2 \nabla \nabla^2 h) \cdot \boldsymbol{\nu} = 0$ along the contact line. In this manner, as mentioned in Sec. I, we avoid having to work with transcendental equations like the ones

which arise if such analysis is carried out in 2D [7, 16]. Thus, solving the long-wave model (1) determines how the droplet thickness, h , and contact line position, \mathbf{c} , evolve in time for prescribed contact angles θ , mass flux q , and slip length λ .

In what follows, the free-boundary problem (1) is transformed to a problem defined on a disk of unit radius, centered at $\mathbf{x} = \mathbf{x}_c(t)$ [12]. In principle, the choice for $\mathbf{x}_c(t)$ can be arbitrary as long as it is contained within $\Omega(t)$, so that we are able to define the following one-to-one mapping

$$\mathbf{x} = \mathbf{x}_c(t) + ra(\phi, t)\hat{\mathbf{r}}, \quad (2)$$

where $0 \leq r \leq 1$, $0 \leq \phi < 2\pi$, $a(\phi, t)$ is assumed to be a one-to-one function of ϕ and $\hat{\mathbf{r}} = (\cos \phi, \sin \phi)$. At the contact line, for which $r = 1$, we have that

$$\mathbf{c} = \mathbf{x}_c + a\hat{\mathbf{r}}. \quad (3)$$

With the transformation (2), the original problem (1) reduces to one of determining $h(r, \phi, t)$, $a(\phi, t)$ and $\mathbf{x}_c(t)$ by casting their corresponding PDEs and conditions in the new (r, ϕ) -coordinate system. Lastly, we assume that $\mathbf{x}_c(t)$ evolves such that the origin of the moving frame is always located at the centroid of the wetted area $\Omega(t)$, which requires that

$$\int_0^{2\pi} a^3 \cos \phi \, d\phi = \int_0^{2\pi} a^3 \sin \phi \, d\phi = 0. \quad (4)$$

From Eqs. (4) we are able to obtain an evolution of equation for each of the two components of $\mathbf{x}_c(t)$ (see Ref. [12] for more details on the transformation of the temporal and spatial derivatives in the new coordinate system and the resulting equations for $\dot{x}_c(t)$ and $\dot{y}_c(t)$). As in Part I, we will pursue a combined analytical–numerical approach to deduce lower dimensional models for the evolution of the contact line, given that as λ reduces towards realistically small values, the curvature of the free surface shape steepens near the contact line. Hence, the full problem (1) becomes stiff due to these boundary layers which require denser computational meshes to be resolved, therefore making simulations more demanding [12].

III. MATCHED ASYMPTOTIC ANALYSIS

Just as in the case for droplets of constant volume [12], we assume that $a \gg \partial_\phi a$, expanding $a(\phi, t)$ as a truncated Fourier series of the form

$$a(\phi, t) = \sum_{m=0}^M a_m(t) e^{im\phi}, \quad (5)$$

where a_m are generally complex functions of t to be determined, with $|a_m(t)| \ll a_0(t)$, so that $a(\phi, t)$ describes weak perturbations from a circular contact line of radius $a_0(t)$. The series is truncated at $M \ll \lambda^{-1}$, in order to avoid non-physical behaviours that can possibly arise if we allow for variations occurring at lengthscales that are smaller than λ [12]. We note that in the complex series representation (5) and in all expressions containing complex exponentials that are going to be discussed hereinafter are considered with their imaginary parts discarded.

The same assumptions put forth in the analysis of Part I of this study hold, namely that we focus on slow droplet dynamics occurring on the slow time scale $|\ln \lambda|$ as $\lambda \rightarrow 0$, with $|\partial_t \mathbf{c}|$, \dot{v} as well as q to be $O(1/|\ln \lambda|)$. Provided that there is sufficient separation of scales (e.g., for droplets away from equilibrium with $v(t) \gg \lambda$ and $\lambda|\partial_\phi a| \ll 1$), we may develop a lower-dimensional model based on matched asymptotic expansions that adequately capture the dynamics throughout, without having to construct some composite expansion to capture all the pertinent time scales. As in Ref. [12], this entails deducing evolution equations for \mathbf{x}_c and the Fourier coefficients of $a(\phi, t)$ to approximate the corresponding evolution of \mathbf{c} of the full problem (1) as $\lambda \rightarrow 0$. This done by probing separately into the dynamics at the micro-scale, the *inner region*, and the macro-scale, the *outer region*, developing for each region asymptotic expansions for $\partial_\nu h = \boldsymbol{\nu} \cdot \nabla h$ as the other is approached, and obtaining the corresponding evolution equations for \mathbf{c} by matching the two expansions. Although certain parts of the analysis that was carried out in the aforementioned work of Savva *et al.* are applicable in this setting as well, there are some additional terms that arise due to the inclusion of q in Eq. (1) that need to be carefully considered. Thus, to avoid repetition, we merely highlight the key results from Ref. [12], and prompt the reader to refer to that work for further details as appropriate.

Before embarking on the matched asymptotic analysis, it is important to note that, unlike the numerics, \mathbf{x}_c is chosen differently for the analysis. In particular, we require that for any given contact line shape \mathbf{c} , the coordinates \mathbf{x}_c are chosen such that the first harmonic of $a(\phi, t)$ is always suppressed so that $a_1(t) \equiv 0$. Uniquely defining \mathbf{x}_c in this manner is always possible for all one-to-one functions $a(\phi, t)$. Why this choice is the natural one for the analysis becomes apparent when considering the outer region dynamics, see Sec. III B.

A. Inner region

The dynamics of the inner region may be examined by sufficiently zooming into the vicinity of the contact line through the appropriate stretching transformations. Given that, by assumption, $q(\mathbf{c}, t) = 0$, mass flux effects contribute to the $O(\lambda)$ terms, which are neglected here. Hence, the analysis is identical to the inner region asymptotics for droplets of constant volume [12]. The key idea behind the inner region asymptotics in 3D is that if $|\partial_t \mathbf{c} \cdot \boldsymbol{\nu}| \gg \lambda$ and the contact line varies at lengthscales that are longer than slip (equivalently, $\lambda|\partial_\phi a| \ll 1$ and $\lambda|\partial_\phi^2 a| \ll 1$), the analysis of the inner region is, at leading-order as $\lambda \rightarrow 0$, the same as in the 2D geometry [20]. This gives rise to the following two-term expansion for the inner region, h_{in} ,

$$-\partial_\nu h_{\text{in}} \sim \theta_* + \frac{\partial_t \mathbf{c} \cdot \boldsymbol{\nu}}{\theta_*^2} \ln \left[\frac{e\theta_*(\mathbf{c} - \mathbf{x}) \cdot \boldsymbol{\nu}}{\lambda} \right] + \dots \quad \text{as} \quad \frac{(\mathbf{c} - \mathbf{x}) \cdot \boldsymbol{\nu}}{\lambda} \rightarrow \infty, \quad (6)$$

where the dots denote higher-order corrections which are omitted. Combining Eqs. (3) and (5), and noting that $\boldsymbol{\nu} = \hat{\mathbf{r}} - \partial_\phi a \hat{\boldsymbol{\phi}}/a_0 + \dots$, we can produce an expansion for $\partial_t \mathbf{c} \cdot \boldsymbol{\nu}$ in the limit of nearly circular contact lines as

$$\partial_t \mathbf{c} \cdot \boldsymbol{\nu} = \dot{b}_0 + \left(\dot{b}_1 - \frac{b_2 \dot{b}_1^*}{b_0} \right) e^{i\phi} + \left(\dot{b}_2 - \frac{3b_3 \dot{b}_1^*}{2b_0} \right) e^{2i\phi} + \sum_{m=3}^M \left[\dot{b}_m + \frac{(m-1)b_{m-1}}{2b_0} \dot{b}_1 - \frac{(m+1)b_{m+1}}{2b_0} \dot{b}_1^* \right] e^{im\phi} + \dots \quad (7)$$

where dots denote differentiation with respect to t , b_1^* is the complex conjugate of b_1 , and b_m are defined through

$$b_m(t) = \begin{cases} x_c(t) - iy_c(t), & \text{for } m = 1 \\ a_m(t), & \text{for } m \neq 1 \end{cases}, \quad (8)$$

with $b_{M+1} = 0$ and $\mathbf{x}_c(t) = (x_c(t), y_c(t))$. It is thus clear that by letting $a_1(t) \equiv 0$, the $e^{i\phi}$ terms are associated with the origin of the moving frame through $b_1(t)$. Although for such a choice the contact line shape is no longer centred at the centroid of the drop, Eq. (5) in Eqs. (4) gives $\text{Re}(a_1) + O(a_m^2) = \text{Im}(a_1) + O(a_m^2) = 0$, readily implying that the two choices are equivalent to each other, at least within the orders of terms retained in the asymptotics. Using Eq. (7), we can write Eq. (6) in terms of the moving polar coordinates system, Eq. (2), which is to be matched with the corresponding outer-region expansion. In the end, we find

$$-\partial_\nu h_{\text{in}} \sim \theta_* + \frac{1}{\theta_*^2} \ln \left(eb_0 \bar{\theta}_* \frac{1-r}{\lambda} \right) \left\{ \dot{b}_0 + \left(\dot{b}_1 - \frac{b_2 \dot{b}_1^*}{b_0} \right) e^{i\phi} + \left(\dot{b}_2 - \frac{3b_3 \dot{b}_1^*}{2b_0} \right) e^{2i\phi} + \sum_{m=3}^M \left[\dot{b}_m + \frac{(m-1)b_{m-1}}{2b_0} \dot{b}_1 - \frac{(m+1)b_{m+1}}{2b_0} \dot{b}_1^* \right] e^{im\phi} \right\}, \quad \text{as} \quad \frac{b_0(1-r)}{\lambda} \rightarrow \infty, \quad (9)$$

where

$$\bar{\theta}_* = \frac{1}{2\pi} \int_0^{2\pi} \theta(\mathbf{c}) d\phi, \quad (10)$$

denotes the average value of θ along the contact line.

B. Outer region

In the outer region, slip effects are negligible so that we may drop $O(\lambda)$ terms in (1), namely

$$\partial_t h_{\text{out}} - (\dot{\mathbf{x}}_c + r \partial_t a \hat{\mathbf{r}}) \cdot \nabla h_{\text{out}} + \nabla \cdot (h_{\text{out}}^3 \nabla \nabla^2 h_{\text{out}}) = q, \quad (11)$$

which is solved subject to the conditions

$$h_{\text{out}}(1, \phi, t) = 0, \quad (12a)$$

$$\frac{d}{dt} \int_0^{2\pi} \int_0^1 r a^2 h_{\text{out}} dr d\phi = \int_0^{2\pi} \int_0^1 r a^2 q dr d\phi = \dot{v}(t). \quad (12b)$$

Next we introduce the quasistatic expansion

$$h_{\text{out}}(r, \phi, t) = h_0(r, \phi, t) + h_1(r, \phi, t) + \dots, \quad (13)$$

where $h_0 \gg h_1$ and h_1 is assumed to be linear in $\dot{b}_m(t)$ and $\dot{v}(t)$ terms. The first term, h_0 , is cast as

$$h_0(r, \phi, t) = h_{0,0}(r, b_0) + \sum_{m=2}^M b_m(t) h_{0,m}(r, b_0) e^{im\phi} + \dots, \quad (14)$$

and describes the leading-order shape of the droplet in the bulk. The functions $h_{0,0}$ and $h_{0,m}$ are determined from the quasi-equilibrium problem

$$\nabla^2 h_0(r, \phi, t) = k(t), \quad (15a)$$

$$h_0(1, \phi, t) = 0, \quad (15b)$$

$$\int_0^{2\pi} \int_0^1 r a^2 h_0 dr d\phi = v(t), \quad (15c)$$

where $k(t)$ is found from the volume constraint, Eq. (1e). We note that flux terms do not appear in Eqs. (15), since $q = O(1/|\ln \lambda|)$ by assumption and, as a result, such terms are treated as a higher-order effect. A series solution to Eq. (15) is obtained perturbatively in the form

$$h_0 = \bar{\vartheta} \left[\frac{b_0(1-r^2)}{2} + \sum_{m=2}^M b_m (r^m - r^2) e^{im\phi} \right] + \dots, \quad (16)$$

where $\bar{\vartheta}(t) = 4v(t)/(\pi b_0^3)$ denotes the (time-dependent) average value of the apparent contact angle ϑ , which may be determined from the normal derivative of h_0 and is expanded as

$$\vartheta = \partial_\nu h_0|_c = \bar{\vartheta} \left[1 + \sum_{m=2}^M \frac{b_m(1-m)}{b_0} e^{im\phi} \right] + \dots \quad (17)$$

The next order term, h_1 , is a correction that captures the contributions due to the mass flux as well as the contact line velocities, and satisfies

$$\partial_t h_0 - (\dot{\mathbf{x}}_c + r \partial_t a \hat{\mathbf{r}}) \cdot \nabla h_0 + \nabla \cdot (h_0^3 \nabla \nabla^2 h_1) = q, \quad (18a)$$

with

$$h_1(1, \phi, t) = 0, \quad \int_0^{2\pi} \int_0^1 r a^2 h_1 dr d\phi = 0, \quad \int_0^{2\pi} \int_0^1 r a^2 q dr d\phi = \dot{v}(t). \quad (18b,c,d)$$

Writing

$$h_1(r, \phi, t) = \sum_{m=0}^M h_{1,m}(r, t) e^{im\phi}, \quad (19)$$

we wish to produce a series of linear problems for $h_{1,m}$. To proceed, consider in Eq. (18a)

$$\partial_t h_0 = \dot{v} \partial_\nu h_0 + \dot{b}_0 \partial_{b_0} h_{0,0} + \sum_{m=2}^M \dot{b}_m h_{0,m} e^{im\phi} + \dots \quad (20)$$

and the truncated Fourier series

$$q(r, \phi, t) = \dot{v} \sum_{m=0}^M q_m(r, t) e^{im\phi}, \quad (21)$$

where $q_m(1, t) = 0$ (because, by assumption, $q \rightarrow 0$ as $\mathbf{x} \rightarrow \mathbf{c}$) and that

$$\sum_{m=0}^M \int_0^{2\pi} \int_0^1 r a^2 q_m(r, t) e^{im\phi} dr d\phi = 1, \quad (22)$$

which follows from Eq. (1e). Collecting $e^{im\phi}$ terms gives rise to a set of decoupled differential equations for $h_{1,m}$ of the form

$$\mathcal{L}_m p_m + 8A_m = 0, \quad (23)$$

where

$$p_m = \frac{1}{r} \partial_r (r \partial_r h_{1,m}) - \frac{m^2}{r^2} h_{1,m}, \quad (24)$$

$$A_m(r, t) = \frac{b_0 r}{\vartheta^2} \times \begin{cases} \dot{b}_0 (2r^2 - 1) - \frac{\dot{\vartheta}}{\vartheta} \left[q_0 - \frac{2(1-r^2)}{b_0^2 \pi} \right], & m = 0, \\ \dot{b}_m r^m - \frac{r(m+1)b_{m+1}}{2b_0} \dot{b}_1^* - \frac{\dot{\vartheta}}{\vartheta} q_m, & m = 1 \text{ or } 2, \\ \dot{b}_m r^m + \frac{r(m-1)b_{m-1}}{2b_0} \dot{b}_1 - \frac{r(m+1)b_{m+1}}{2b_0} \dot{b}_1^* - \frac{\dot{\vartheta}}{\vartheta} \left[q_m - \frac{4b_m(r^m - r^2)}{b_0^3 \pi} \right], & m > 2, \end{cases} \quad (25)$$

and \mathcal{L}_m is the self-adjoint differential operator

$$\mathcal{L}_m(\cdot) = \partial_r \left[r(1-r^2)^3 \partial_r(\cdot) \right] - m^2 r^{-1} (1-r^2)^3(\cdot). \quad (26)$$

The asymptotics of Eq. (23) reveals that $p_m \sim A_m(1, t)/(1-r)$ as $r \rightarrow 1$, or, equivalently,

$$-\partial_r h_{1,m} \sim A_m(1, t) \ln(1-r) + B_m(t) \quad \text{as } r \rightarrow 1^-, \quad (27)$$

for $m \geq 0$. A two-term asymptotic expansion requires determining $B_m(t)$, which can be accomplished by following a similar approach as in Part I. Specifically, for each harmonic $m \geq 0$, we multiply Eq. (23) by some function $f_m(r)$ to be determined, and integrate over r from 0 to $1-\epsilon$, $0 < \epsilon \ll 1$. By choosing $f_m(r)$ so that the boundary terms arising from repeated integration by parts vanish, we get

$$\int_0^{1-\epsilon} p_m(r, t) \mathcal{L}_m f_m(r) dr = -8 \int_0^{1-\epsilon} A_m(r, t) f_m(r) dr. \quad (28)$$

When $m \neq 0$, the boundary terms vanish if $r f_m(r) < \infty$ as $r \rightarrow 0$ and f_m has (at worst) a simple pole as $r \rightarrow 1$. If, in addition, we require for $m \neq 0$ that

$$\mathcal{L}_m f_m(r) + 8r^{m+1} = 0, \quad (29)$$

we may use Eq. (24) to simplify the left hand side of Eq. (28) so that

$$A_m(1, t) \ln \epsilon + B_m(t) + O(\epsilon \ln \epsilon) = - \int_0^{1-\epsilon} A_m(r, t) f_m(r) dr, \quad (30)$$

which is accomplished through integration by parts and substituting the asymptotics of $\partial_r h_{1,m}$, Eq. (27). Since

$$\ln \epsilon = - \int_0^{1-\epsilon} \frac{1}{1-r} dr, \quad (31)$$

we replace this expression for $\ln \epsilon$ in Eq. (30). After term rearrangement, we take the limit $\epsilon \rightarrow 0$, which yields $B_m(t)$ in integral form, namely

$$B_m(t) = \int_0^1 \left(\frac{A_m(1, t)}{1-r} - A_m(r, t) f_m(r) \right) dr. \quad (32)$$

The latter expression can be cast in the form

$$B_m(t) = \frac{b_0}{\vartheta^2} \left\{ \dot{b}_m \beta_m + \left(\frac{(m-1)b_{m-1} \dot{b}_1}{2b_0} - \frac{(m+1)b_{m+1} \dot{b}_1^*}{2b_0} \right) \gamma_m + \frac{\dot{\vartheta} \zeta_m}{\vartheta} \right\}, \quad (33)$$

when $m > 2$ and

$$B_m(t) = \frac{b_0}{\vartheta^2} \left\{ \dot{b}_m \beta_m - \frac{(m+1)b_{m+1}\dot{b}_1^*}{2b_0} \gamma_m + \frac{\dot{\zeta}_m}{\vartheta} \right\}, \quad (34)$$

when $m = 1$ or 2 , where

$$\beta_m = \int_0^1 \left(\frac{1}{1-r} - f_m(r)r^{m+1} \right) dr, \quad (35)$$

$$\gamma_m = \int_0^1 \left(\frac{1}{1-r} - f_m(r)r^2 \right) dr, \quad (36)$$

$$\zeta_m(t) = \int_0^1 r f_m(r) \left(q_m(r, t) - \frac{4b_m(t)(r^m - r^2)}{b_0^3(t)\pi} \right) dr, \quad (37)$$

for all $m \geq 1$. Therefore, for given $f_m(r)$ satisfying Eq. (29) with $f_m(0) = 0$ and $f_m \sim 1/(1-r)$ as $r \rightarrow 1$, the parameters β_m , γ_m and $\zeta_m(t)$ may be evaluated numerically for $m > 0$. The solution to Eq. (29) is

$$f_m(r) = \frac{4r^m}{(m+4)(1-r^2)^2} \left[\frac{g_m(r^2)}{g_m(1)} - 1 \right], \quad m \geq 1 \quad (38)$$

where $g_m(r)$ is the Gauss hypergeometric function

$$g_m(r) = {}_2F_1 \left(\frac{m-1-\sqrt{m^2+9}}{2}, \frac{m-1+\sqrt{m^2+9}}{2}; m+1; r \right). \quad (39)$$

The parameters β_m and γ_m are computed once using Gauss–Legendre quadrature, stored and retrieved whenever needed in simulations. The time-dependent $\zeta_m(t)$ are computed at each time step using the same quadrature rule. For efficiency in their evaluation, we pre-compute the $f_m(r)$ and re-use them at each time step. The general approaches used are detailed in Ref. [12]. It turns out that the values of the γ_m 's in the present paper are the same as the $\tilde{\beta}_m$'s in Ref. [12], noting a typo in Eq. (6.13) of Ref. [12], where the $8r^2$ should have been $8r^3$.

The case when $m = 0$ follows in a similar manner, once we recognize that $h_{1,0}$ must also satisfy $\int_0^1 r h_{1,0} dr = 0$, which follows directly from the series expansion of Eq. (18b). Given the freedom we can afford in choosing what $\mathcal{L}_0 f_0$ equals to in Eq. (28), it turns out that by letting $\mathcal{L}_0 f_0 = 8r(1-2r^2)$, we can explicitly enforce this condition in the subsequent integrations by parts applied to Eq. (28) to yield Eq. (30). In this case, solving $\mathcal{L}_0 f_0 = 8r(1-2r^2)$ with the same conditions satisfied by $f_m(r)$, $m \geq 0$, gives

$$f_0(r) = \frac{2r^2}{1-r^2}, \quad (40)$$

so that we may deduce $B_0(t)$ from (28) as

$$B_0(t) = \int_0^1 \frac{1}{1-r} \left(A_0(1, t) - \frac{2r^2 A_0(r, t)}{1+r} \right) dr. \quad (41)$$

Hence, using the expression for $A_0(t)$, $B_0(t)$ may be written as

$$B_0(t) = \frac{b_0}{\vartheta^2} \left\{ \dot{b}_0 \beta_0 + \frac{\dot{\zeta}_0}{\vartheta} \right\}, \quad (42)$$

where

$$\beta_0 = 2 + \ln 2 \quad \text{and} \quad \zeta_0(t) = -\frac{1}{\pi b_0^2} + 2 \int_0^1 \frac{r^3 q_0(r)}{1-r^2} dr. \quad (43)$$

From the above considerations, we can produce a two-term expansion of $\partial_\nu h_{\text{out}}$ as $r \rightarrow 1^-$ using Eqs. (19) and (27), namely

$$-\partial_\nu h_{\text{out}} \sim \vartheta + \frac{1}{\vartheta^2} \sum_{m=0}^M [A_m(1, t) \ln(1-r) + B_m(t)] e^{im\phi}. \quad (44)$$

C. Matching

As in the 2D analysis conducted in Part I with vanishing fluxes at the contact points, we may asymptotically match the cubes of the inner and outer normal derivatives given by Eqs. (9) and (44), respectively, so that they become

$$-(\partial_\nu h_{\text{in}})^3 \sim \theta_*^3 + 3 \ln \left(eb_0 \bar{\theta}_* \frac{1-r}{\lambda} \right) \sum_{m=0}^M A_m(1, t) e^{im\phi} \quad \text{as} \quad \frac{1-r}{\lambda} \rightarrow \infty, \quad (45)$$

$$-(\partial_\nu h_{\text{out}})^3 \sim \vartheta^3 + 3 \sum_{m=0}^M [A_m(1, t) \ln(1-r) + B_m(t)] e^{im\phi} \quad \text{as} \quad r \rightarrow 1^-. \quad (46)$$

Within the appropriate overlap region, $(\partial_\nu h_{\text{in}})^3 \sim (\partial_\nu h_{\text{out}})^3$ [21], which allows us to eliminate the $\ln(1-r)$ terms to deduce a Cox–Voinov-type evolution equation for the contact line

$$\frac{\vartheta^3 - \theta_*^3}{3} = \sum_{m=0}^M \left(A_m(1, t) \ln \frac{eb_0 \bar{\theta}_*}{\lambda} - B_m(t) \right) e^{im\phi}. \quad (47)$$

Letting

$$\tilde{\beta}_m(t) = \ln \frac{eb_0 \bar{\theta}_*}{\lambda} - \beta_m \quad \text{and} \quad \tilde{\gamma}_m(t) = \ln \frac{eb_0 \bar{\theta}_*}{\lambda} - \gamma_m, \quad (48)$$

we may expand Eq. (47) to get

$$\begin{aligned} \frac{\vartheta^3 - \theta_*^3}{3} &= \tilde{\beta}_0 \dot{b}_0 - \zeta_0 \dot{v} + \left[\tilde{\beta}_1 \dot{b}_1 - \zeta_1 \dot{v} - \frac{b_2 \tilde{\gamma}_1}{b_0} \dot{b}_1^* \right] e^{i\phi} + \left[\tilde{\beta}_2 \dot{b}_2 - \zeta_2 \dot{v} - \frac{3b_3 \tilde{\gamma}_2}{2b_0} \dot{b}_1^* \right] e^{2i\phi} \\ &+ \sum_{m=3}^M \left\{ \tilde{\beta}_m \dot{b}_m - \zeta_m \dot{v} + \tilde{\gamma}_m \left[\frac{(m-1)b_{m-1}}{2b_0} \dot{b}_1 - \frac{(m+1)b_{m+1}}{2b_0} \dot{b}_1^* \right] \right\} e^{im\phi}. \end{aligned} \quad (49)$$

Assuming a truncated Fourier Series expansion for the left hand side

$$\frac{\vartheta^3 - \theta_*^3}{3} = \sum_{m=0}^M w_m e^{im\phi}, \quad (50)$$

allows us to deduce the pertinent system of equations for the evolution of the harmonics of the contact line

$$\tilde{\beta}_0 \dot{b}_0 = w_0 + \zeta_0 \dot{v}, \quad (51a)$$

$$\tilde{\beta}_1 \dot{b}_1 - \frac{b_2 \tilde{\gamma}_1}{b_0} \dot{b}_1^* = w_1 + \zeta_1 \dot{v}, \quad (51b)$$

$$\tilde{\beta}_2 \dot{b}_2 - \frac{3b_3 \tilde{\gamma}_2}{2b_0} \dot{b}_1^* = w_2 + \zeta_2 \dot{v}, \quad (51c)$$

$$\tilde{\beta}_m \dot{b}_m + \frac{(m-1)b_{m-1} \tilde{\gamma}_m}{2b_0} \dot{b}_1 - \frac{(m+1)b_{m+1} \tilde{\gamma}_m}{2b_0} \dot{b}_1^* = w_m + \zeta_m \dot{v} \quad \text{for} \quad m \geq 3. \quad (51d)$$

The reduced system of equations (51) describes fully the leading-order droplet spreading dynamics as $\lambda \rightarrow 0$, confirming *a posteriori* the assertion that both $|\dot{v}|$ and $|\dot{b}_m|$ are $O(1/|\ln \lambda|)$ as $\lambda \rightarrow 0$. Like the 2D analysis, when

$$q = \dot{v}h/v, \quad (52)$$

we may eliminate the $\dot{v}(t)$ terms from Eqs. (51) so that volume changes appear only through the apparent contact angle (17), and therefore arrive with the same equations deduced in Ref. [12]. Further simplifications can be obtained by neglecting $O(\dot{b}_1 b_m)$ and $O(\dot{b}_1^* b_m)$ terms in the expansion of $\partial_t \mathbf{c} \cdot \boldsymbol{\nu}$, which are nevertheless smaller than $O(\dot{b}_m)$ terms. This change essentially corresponds to setting $\tilde{\gamma}_m$ terms to zero in Eqs. (51). Although such terms correspond to higher-order corrections of the centroid motion, we chose to retain these terms in all cases explored, since they may accumulate non-negligible contributions when multiple periods of inflow/outflow are considered.

IV. RESULTS

In this section we assess the outcomes of the asymptotic analysis of the preceding section through a series of numerical experiments which compare the predictions of Eqs. (51) with those of the governing equation and the appropriate initial conditions, Eqs. (1), hereinafter referred to as the *full model*. Central to the calculations using the asymptotic model, Eqs. (51), is the way the apparent contact angle, ϑ , is evaluated. Once ϑ is known, the system constitutes a set of generally weakly coupled and non-stiff integrodifferential equations and their implementation is relatively straightforward. It is decomposed into $2M + 1$ unknowns for the evolution of b_0 and the real and imaginary parts of b_m , $m = 1, 2, \dots, M$ (considering $M = 50$ is typically sufficient, unless the structure of the heterogeneities has small-scale features). The whole process involves moving back and forth in Fourier space while time stepping is performed with a standard ordinary differential equation integrator, coupled with numerical quadrature for computing the time-dependent integrals $\zeta_m(t)$ (see Sec. IIIB).

Just as in Ref. [12], ϑ is computed using two different methods. The first is based on the perturbative approximation of ϑ given by Eq. (17) and this model is referred to as *reduced*. Through the second approach, ϑ is determined more accurately for a given contact line shape, by solving Eqs. (15) with the boundary integral method. In this manner, we formulate a linear integral equation which outputs ϑ by solving a linear system. Since this approach leverages the simpler system (51) with the numerical solution of a PDE, the resulting model is referred to as *hybrid*. The general methodologies adopted for solving the full, reduced and hybrid models, and for computing the associated integral terms are described in Ref. [12].

Unless stated otherwise, we consider cases for which $\lambda = 10^{-3}$, fix $a(\phi, 0) = 1$, $\mathbf{x}_c(0) = \mathbf{0}$, and plot solutions to the full, hybrid, and reduced models with solid, dashed and dotted curves, respectively. Likewise, in all cases where $\theta(\mathbf{x})$ is represented by shading regions of the x - y plane, darker/lighter shades correspond to larger/smaller contact angles. Just like the 2D case, in some simulations we consider volume fluctuations according to

$$v(t) = \bar{v} - \frac{\tilde{v}}{\arctan 20} \arctan \left[\frac{20 \cos(2\pi t/p)}{\sqrt{1 + 400 \sin^2(2\pi t/p)}} \right], \quad (53)$$

which describes a p -periodic triangular wave with $\bar{v} - \tilde{v} \leq v(t) \leq \bar{v} + \tilde{v}$ (see, e.g., Fig. 9), noting that a similar form shifted by $p/4$ was introduced in Part I (see Eq. (34), Part I). It is important to note that λ takes larger values than those in Part I simply because the full problem becomes increasingly stiff as $\lambda \rightarrow 0$, thus requiring significantly more computational resources to be simulated. Also noteworthy is that, in most cases, the chemical heterogeneities $\theta(\mathbf{x})$ considered do not vary too sharply in order to avoid issues with retracting contact lines. In such cases, the contact line may develop protrusions which become elongated as the contact line retracts. Such features cannot be adequately resolved by the numerical scheme adopted and adaptive meshing techniques would be required. We chose not to pursue this route, since the validity of the analysis undertaken would be rather questionable in such cases.

A. Random substrates

The first example we consider is motivated by the experiments performed by Dietrich *et al.* who investigate the evaporation of alcohol droplets in air, where they report four evaporation modes, namely the constant contact angle and constant contact radius modes, as well as stick-slide and stick-jump modes, the latter of which is caused by the intermittent pinning of the contact line [3]. The analysis presented in Sec. III does not account for evaporation, because the mass flux is maximized near the contact line [17–19]. However, one can qualitatively reproduce such a situation by considering a simple linear mass loss with Eq. (52) for the distribution of the flux. To induce a non-trivial centroid motion, we prescribe noisy chemical heterogeneities of the form

$$\theta(\mathbf{x}) = \hat{\theta}(\mathbf{x}) + \tilde{\theta}(\mathbf{x}), \quad (54)$$

where $\hat{\theta}(\mathbf{x})$ is a deterministic part giving the dominant structure of the substrate, and $\tilde{\theta}(\mathbf{x})$ corresponds to a realization of spatial band-limited white noise. In Part I of this study, similar substrates were considered for exploring the snapping dynamics observed by Wells *et al.* [6] (see Fig. 10 in Part I).

Fig. 2 shows a case of a substrate with heterogeneities of the form (54), where $\hat{\theta}(\mathbf{x}) \equiv 1.5$ and $\tilde{\theta}(\mathbf{x})$ is represented by a superposition of 75 harmonics with wavenumbers up to 3π and whose amplitudes are normally distributed with zero mean and unit variance, ensuring that $\theta(\mathbf{x}) > 0$ everywhere. By tracking the mean values of $a(\phi, t)$, b_0 , and the apparent contact angle ϑ , $\bar{\vartheta}$, we observe behaviors that are qualitatively similar to the observations recorded in Fig. 2 of [3], noting that we used $h_{\max} = b_0 \bar{\vartheta}/2$ as a proxy for the maximum height of the droplet, found by setting $r = 0$ in

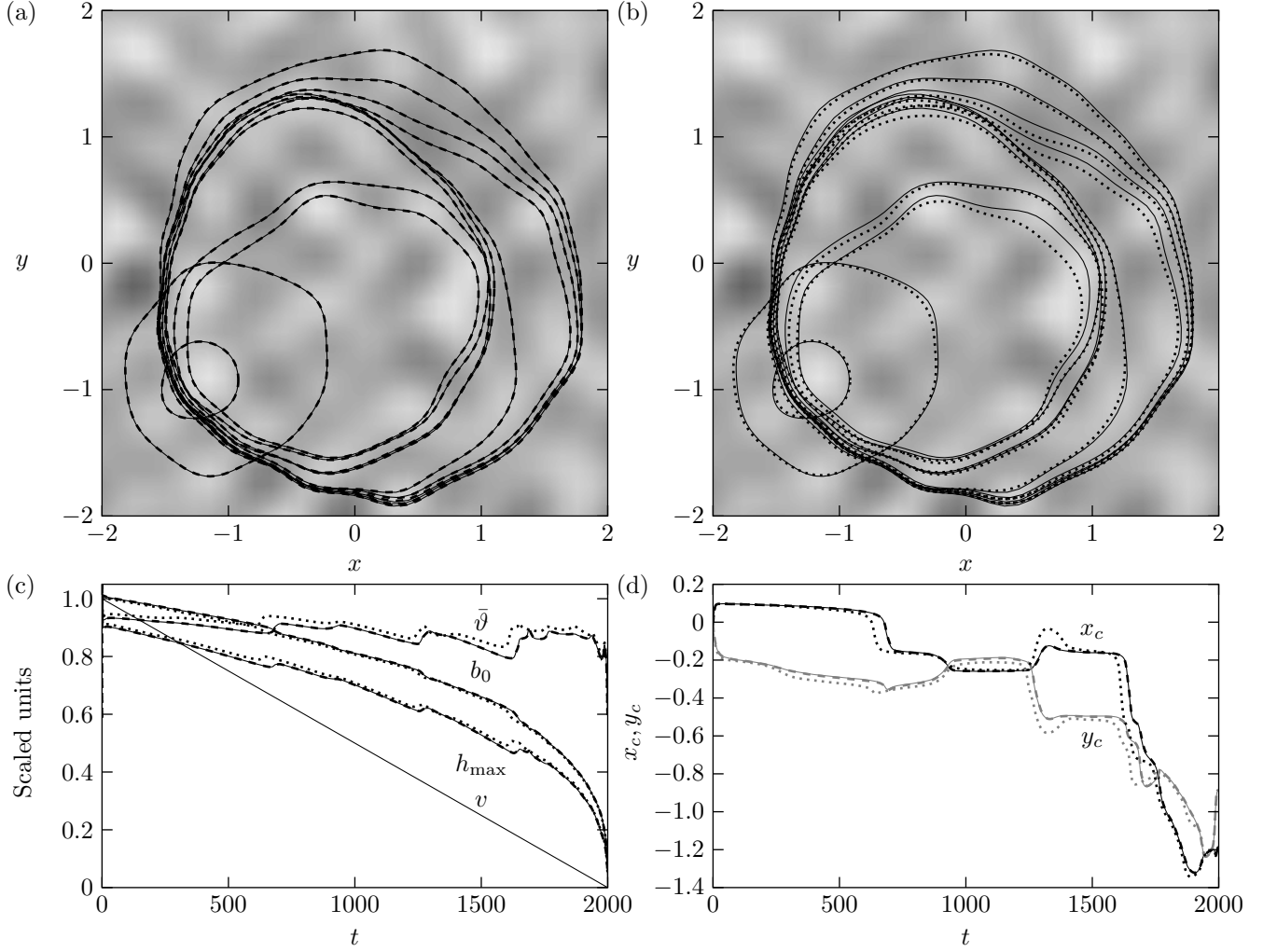


FIG. 2. Stick-slip dynamics on a randomly varying $\theta(\mathbf{x})$ (see text for more details on how the profile is generated) with $v(t) = \pi(2 - 0.001t)$ and $q(\mathbf{x}, t)$ prescribed according to Eq. (52). (a) and (b) show contact line profiles when $t = 10, 200, 400, 600, 800, 1000, 1200, 1400, 1600, 1800$ and 1990 , comparing the solutions to the full problem with the hybrid and reduced problems, respectively (darker shades correspond to larger contact angles). (c) Evolution of the mean radius b_0 , mean macroscopic angle $\bar{\vartheta}$, maximum height h_{\max} , and volume v , each scaled by $1.7, 1.7, 1.5$ and 2π , respectively. (d) The evolution of the centroid coordinates, x_c (black) and y_c (gray). In all plots, the solid, dashed and dotted curves correspond to solutions to the full, hybrid and reduced problems, respectively.

Eq. (16). Although the corresponding measurements in experiments are usually taken from photographs of the side of the droplet, recording the mean values of a and ϑ from nearly circular contact lines as done here gives similar results (see the contact line profiles in Fig. 2(a)).

As the droplet loses mass, its mean radius exhibits a series of jumps which is also marked with a temporary increase in h_{\max} and $\bar{\vartheta}$. Usually in these circumstances the contact line will locally remain pinned at a lower wettability region, thus causing other parts of the contact line to respond to this pinning by shifting towards the pinning site as the droplet loses mass (see Figs. 2(a), (b) and (d)). Once the contact line manages to overcome this wettability barrier, it exhibits a stick-jump event. These behaviors corroborate the experimental observations of Dietrich *et al.* [3] which were also attributed to spatial variations in surface heterogeneities. Noteworthy also is the excellent agreement between the predictions offered by the full and hybrid models which shows nearly indistinguishable results. The reduced model on the other hand shows some disagreement, but captures the generic features reasonably well.

One of the key observations of Part I of the present study was that periodic variations in the droplet mass led to periodic 2D droplet dynamics after the decay of initial transients, which typically occur within three to four periods. To assess how well this applies in the 3D setting, we use a substrate with random heterogeneities prescribed according to Eq. (54) with $\hat{\theta}(\mathbf{x}) = 1$ and where $\tilde{\theta}(\mathbf{x})$ is a superposition of 10 harmonics with wavenumbers up to 2π , whose

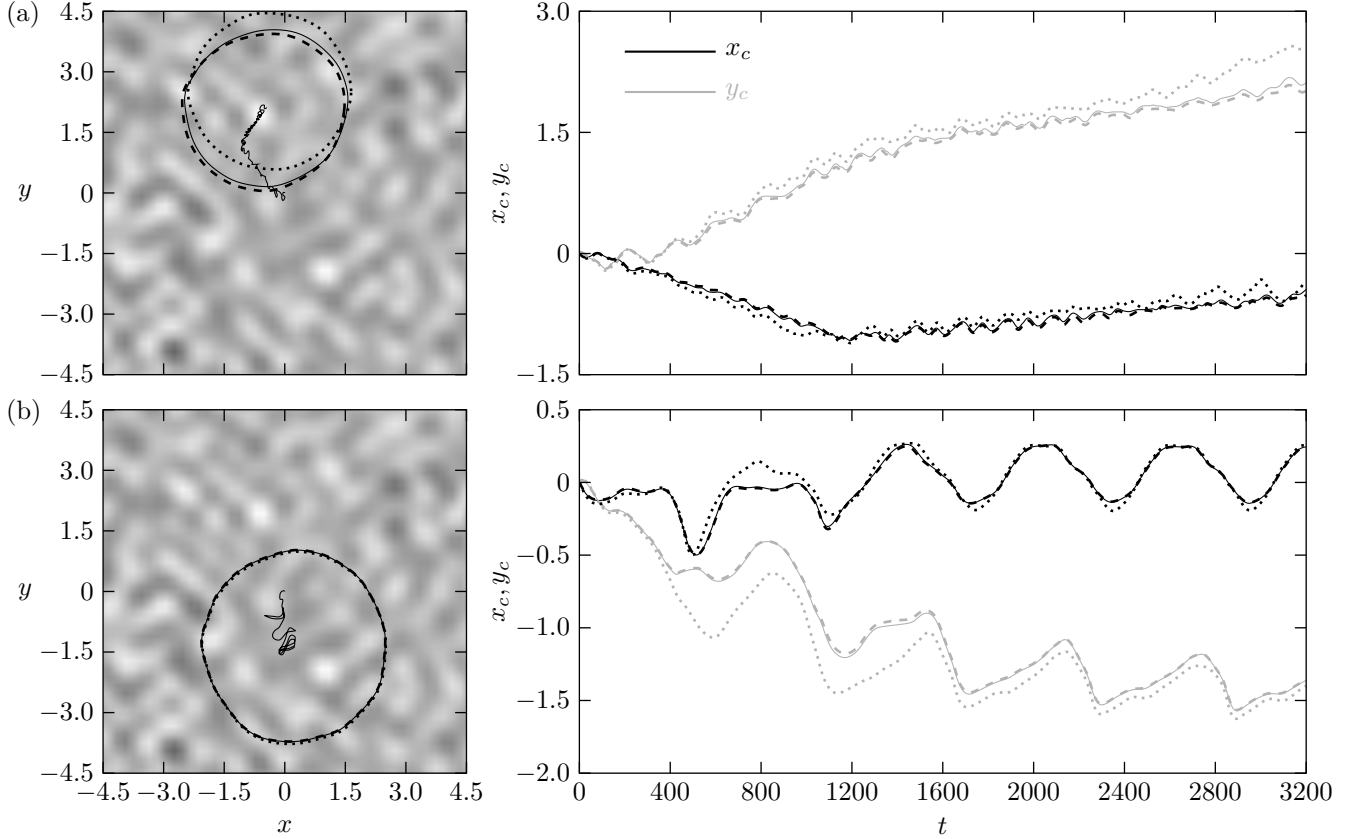


FIG. 3. Periodic variations in droplet volume over a substrate comprised of randomized heterogeneous features (see text for a brief description on how the substrate is generated), where $v(t)$ prescribed according to Eq. (53) with t being replaced with $t + p/4$, $\bar{v} = 2\pi$, $\tilde{v} = 1.5\pi$ and $q(\mathbf{x}, t)$ according to Eq. (52). For panel (a), $p = 200$; for panel (b), $p = 600$. In each panel, the left plot shows the contact line shape at $t = 3200$ for the full model (solid curves) hybrid model using Eqs. (51) (dashed curves) and the hybrid model using Eq. (55) (dotted curves), and the path followed by $\mathbf{x}_c(t)$; the right plot shows the corresponding evolution of the centroid coordinates $x_c(t)$ (black curves) and $y_c(t)$ (dotted curves).

amplitudes are normally distributed with zero mean and variance set to 0.3. For such a substrate, the chemical heterogeneities vary more weakly compared to the substrate used in Fig. 2, giving rise to softer pinning transitions which practically eliminate stick-slip dynamics almost entirely. For this choice for $\theta(\mathbf{x})$ the contact line is more circular, thus requiring fewer collocation points in the azimuthal direction to be accurately resolved and permitting efficient simulations for far larger values of t .

The outcome is shown in Fig. 3, plotting how the centroid evolves for two different values of the period of mass fluctuations, namely $p = 200$ and $p = 600$. Remarkably, the droplets are driven to entirely different locations on the substrate. Moreover, the dynamics when $p = 200$ does not appear to have settled to a periodic state within the simulated time, noting that the agreement of the asymptotic model and the full model progressively degrades. This accumulation of errors may be attributed to two reasons: the first is that longer simulation times became feasible at the expense of lowering the resolution of the computations in the azimuthal direction; the second is that at the instance when q is about to switch from inflow to outflow and vice versa the asymptotic model is no longer valid and the errors may possibly accumulate more quickly for smaller values of p . As mentioned previously as well as in Part I, the asymptotic analysis applies when $\lambda \ll |\partial_t a| \ll 1$ and, strictly speaking, it is rendered invalid when the fronts are about to switch their direction of motion. Hence, these errors coupled with the presence of heterogeneities may mistime stick-slip events, thus moving the droplet to a different location. This situation is arguably exacerbated for the hybrid model based on the leading-order asymptotic theory [14], namely

$$\partial_t \mathbf{c} \cdot \boldsymbol{\nu} = \frac{\theta_*^3 - \vartheta^3}{3 \ln \lambda}, \quad (55)$$

which only captures the $O(1/|\ln \lambda|)$ terms of Eq. (51). Qualitatively, however, neither the hybrid nor the full models appear to settle to a periodic state when $p = 200$. Hence, this result points to the possibility of quasi-periodic

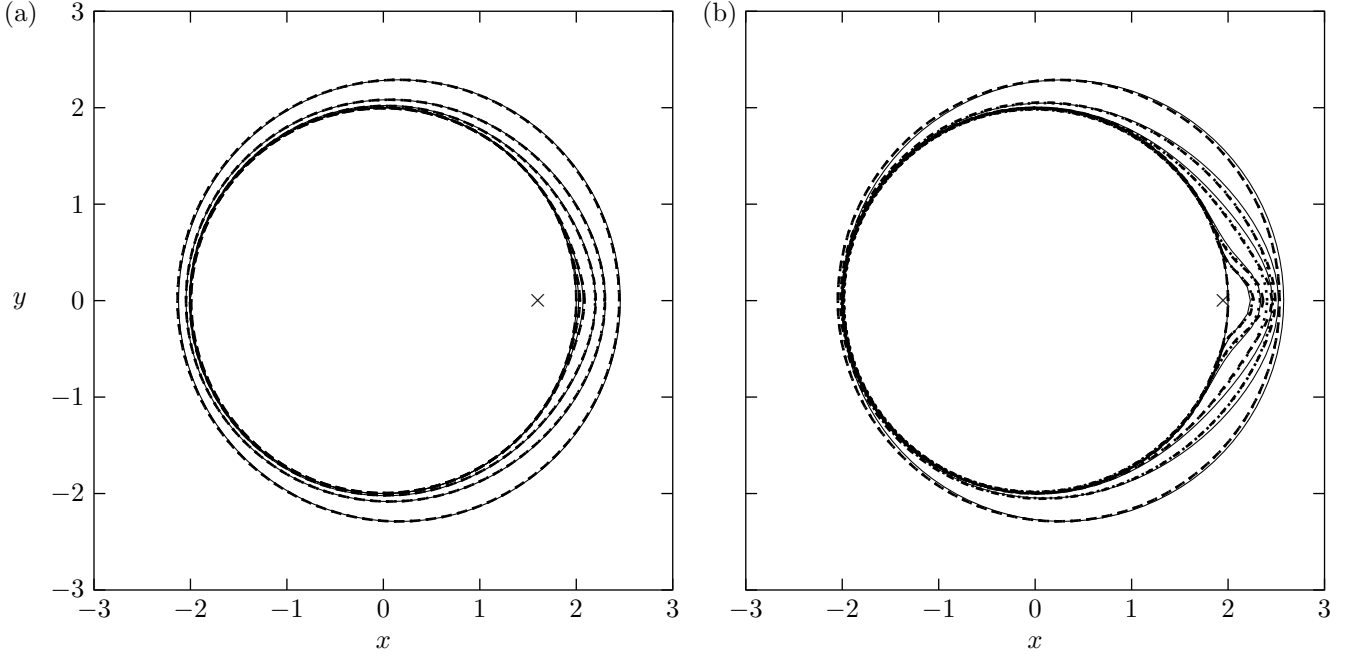


FIG. 4. The effect of localized flux on contact line using (56) with parameters $S = 20$, $(x_0, y_0) = (1.6, 0)$ and $(1.95, 0)$ for (a) and (b), respectively (localization depicted by crosses). The initial contact line shape is prescribed at $a(\phi, 0) = 2$ so that the droplet is at equilibrium for the starting volume $v(0) = 2\pi$. Both plots show droplet profiles at times $t = 0, 0.3, 1, 5, 10$ and 100 over the homogeneous substrate $\theta(\mathbf{x}) = 1$. In both cases volume changes are governed using Eq. (57) with $v_0 = 2\pi$, $v_\infty = 3\pi$ and $\eta = \pi/50$.

dynamics, induced by the non-linear coupling of the random features and the period of inflow/outflow. However, it is expected that larger values of p (e.g., see the case when $p = 600$ in Fig. 3) and/or weaker heterogeneities will mitigate this effect, facilitating the transition to periodic motion as in the 2D case.

B. Localized mass flux

The analysis presented is capable of capturing localized fluxes provided that they vanish within the droplet footprint, $\Omega(t)$. Such types of fluxes have also been explored in Part I, showing that they may reposition the droplet at a different location on the substrate, or even induce topological transitions through break-up. It is thus of interest to look into localized fluxes in the 3D setting as well, firstly by considering a mass flux distribution of the form

$$q = \frac{\dot{v}(t) \exp \left\{ -S \left[(x - x_0)^2 + (y - y_0)^2 \right] \right\}}{\int_{\Omega(t)} \exp \left\{ -S \left[(x - x_0)^2 + (y - y_0)^2 \right] \right\} d\mathbf{x}}, \quad (56)$$

which prescribes a scaled Gaussian, peaking at $(x_0, y_0) \in \Omega(t)$ with $S \gg 1$, noting that the denominator is estimated with numerical quadrature. Just as in Part I, we only consider moderate values of S , chosen as a compromise between the requirement that q vanishes along the contact line while capturing its dynamics with fewer collocation points that would be required to accurately resolve $q(\mathbf{x}, t)$ for much larger values of S . In the examples that follow, we assume that the volume varies according to

$$v(t) = v_0 + (v_\infty - v_0) \tanh(\eta t), \quad (57)$$

which prescribes a volume that monotonically increases from $v = v_0$ at $t = 0$ to $v \rightarrow v_\infty$ as $t \rightarrow \infty$, where $\eta > 0$ is a parameter that controls how fast this transition occurs.

A first example is shown in Fig. 4, where we consider a droplet which is initially centered at the origin, has volume $v(0) = v_0 = 2\pi$ and is at equilibrium on a homogeneous substrate with $\theta(\mathbf{x}) \equiv 1$, i.e. $a(\phi, 0) = 2$. Liquid is pumped

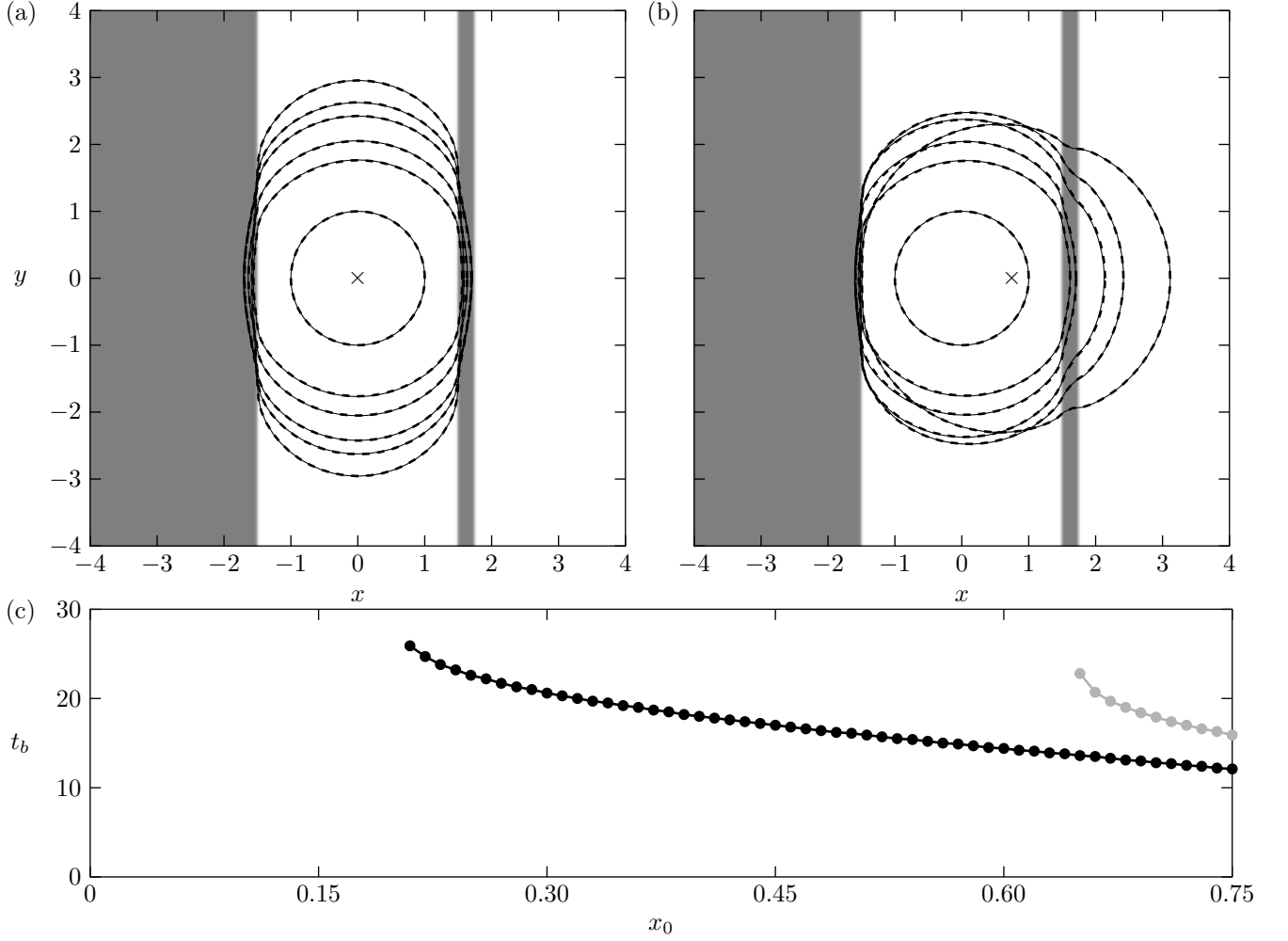


FIG. 5. Localizing the flux from $(x_0, y_0) = (0, 0)$ to $(0.75, 0)$ with the heterogeneous barriers $\theta(x) = 1.2 + \tilde{g} \{ \tanh[50(x - 1.5)] - \tanh[50(x + 1.5)] - \tanh[50(x - 1.75)] \}$. Plots (a) and (b) are droplet profiles at times $t = 0, 5, 10, 20, 30$ and 300 for localization at $x_0 = 0$ and $x_0 = 0.75$, respectively (localization depicted by crosses). The substrate in (a) and (b) is shaded according to the choice of θ where dark and light patches correspond to $\theta \approx 1.2 \pm \tilde{g}$ for $\tilde{g} = 0.25$, respectively. (c) The time the point $x_c(t) + a(0, t)$ breaks the heterogeneous barrier (t_b) against x_0 , where black and gray plots are for $\tilde{g} = 0.25$ and $\tilde{g} = 0.275$, respectively. In all plots volume changes are given by (57) with $v_0 = \pi$, $v_\infty = 3\pi$ and $\eta = \pi/50$.

into the droplet according to q given by Eq. (56) and v by Eq. (57) with $v_\infty = 3\pi$ and $\eta = \pi/50$, for different injection points, namely $(x_0, y_0) = (1.6, 0)$ in Fig. 4(a) and $(x_0, y_0) = (1.95, 0)$ in Fig. 4(b). In both cases, the localization of the flux develops a protrusion at the contact line along the positive x -axis, which becomes more pronounced as the fluid is injected closer to the contact line. Ultimately, however, the contact line relaxes to a circular shape in the long-time limit, as expected. The agreement is slightly less favorable in Fig. 4(b) solely because there is non-negligible mass flux along the contact line in the vicinity of the injection point for the full model, whereas the asymptotic model assumes zero mass flux there.

As already shown in Part I, the interplay of substrate heterogeneities and the way changes in mass occur is rather intricate and small changes to either of them may cause a markedly different behavior. This kind of interplay can be leveraged in applications as a means to control droplet behavior, e.g. for sorting droplets of different sizes (see, e.g. Ref. [22]; also Ref [23] for a review on droplet sorting). Another situation of interest is using mass flux to assist a droplet to escape nearby wettability barriers. This is highlighted in Fig. 5, where we consider a droplet confined between two parallel heterogeneous stripes of lower wettability. Using a localized flux q as prescribed by Eq. (56) and v by Eq. (53), we alter the position of the injection point $(x_0, 0)$ for $x_0 \geq 0$ to determine locations which allow the droplet to escape the rightmost wettability barrier. When x_0 is small, the droplet remains trapped between the two heterogeneous barriers, see e.g. Fig. 5(a). This type of behavior has been reported in related works with droplets of constant mass [24–26]. When x_0 becomes sufficiently large, the droplet may eventually overcome the heterogeneous

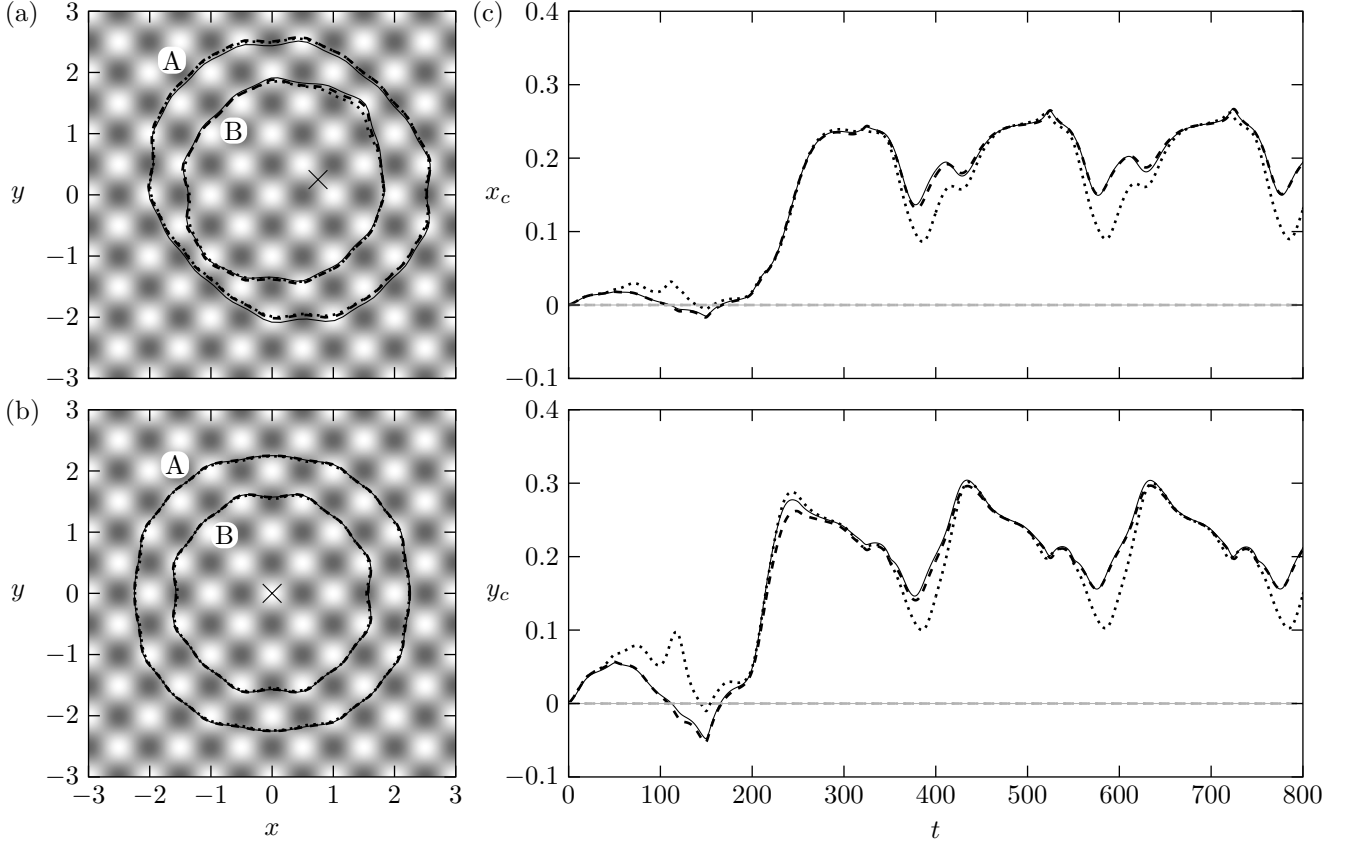


FIG. 6. Transition to periodic dynamics for the substrate with $\theta(\mathbf{x}) = 1 - 0.15 \{ \cos [2\pi(x+y)] + \cos [2\pi(x-y)] \}$. Plots (a) and (b) show the contact line shapes for the full, hybrid and reduced models at $t = 650$ (marked with ‘A’) and $t = 750$ (marked with ‘B’) when $(x_0, y_0) = (0.75, 0.25)$ (plot (a)) and $(x_0, y_0) = (0, 0)$ (plot (b)); the source/sink locations are marked with an \times . The contact line shapes ‘A’ and ‘B’ correspond to the shapes at the maximum/minimum volumes after the droplet settles to a periodic state. Panel (c) shows the evolution of the coordinates of the centroid $x_c(t)$ (top plot) and $y_c(t)$ (bottom plot) when $(x_0, y_0) = (0.75, 0.25)$ (black curves) and $(x_0, y_0) = (0, 0)$ (gray curves). For both cases, the volume varies according to Eq. (53) with t being replaced with $t + p/4$, $\bar{v} = 2\pi$, $\bar{v} = \pi$ and $p = 200$.

barrier (see Fig. 5(b)). These two distinct states are highly dependent both on the value of x_0 and the wettability contrast, see Fig. 5(c). In fact, altering the difference in the local contact angles between the stripes from 0.5 to 0.55 causes a threefold increase in the minimum value of x_0 required to break the barrier, changing $x_0 \approx 0.21$ to $x_0 \approx 0.65$. It is also worth noting that the calculations in Fig. 5(c) were performed with the hybrid model only, where over 100 hybrid-model simulations required far less time to complete than a single full-model simulation.

A feature which persists with the localized flux cases explored is that changing the mass near the contact line can move the droplet preferentially in one direction, sometimes against heterogeneous barriers if these are sufficiently weak, or if the mass flux is sufficiently strong (see Fig. 5). Therefore, mass variations may be used as a mechanism to overcome the energy barriers introduced by chemical heterogeneities. To demonstrate this plausibility, a heterogeneity profile comprising of periodically varying heterogeneous features is considered in Fig. 6. By coupling a localized flux with periodic mass changes, we observe, like in Part I, that the droplet attempts to center itself around the inlet/outlet position of the liquid flux (see also Fig. 7, Part I). However, the presence of heterogeneities may prevent this from happening if these are sufficiently strong (see Fig. 6(a)). Let us also note that, as expected, and in agreement with the observations of Part I, the dynamics ultimately become periodic in the long-time limit as a result of coupling periodic flow conditions and heterogeneous features.

In the limit $S \rightarrow \infty$, Eq. (56) reduces to $q = \dot{v}\delta(x - x_0)\delta(y - y_0)$ where $\delta(x)$ is the Dirac delta function, which in the moving frame is cast in the form

$$q = \frac{\dot{v}(t)\delta(r - r_0)\delta(\phi - \phi_0)}{ra(\phi, t)^2}, \quad (58a)$$

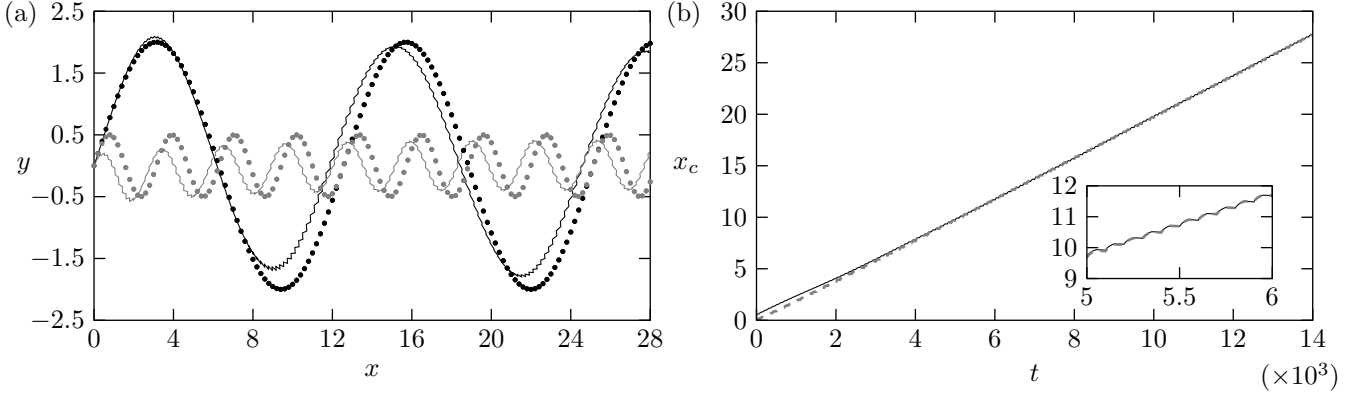


FIG. 7. Droplet transport with the reduced model on a homogeneous substrate, when sinks/sources are positioned along a sinusoidal path according to Eq. (61) with q given by Eq. (60). The droplet is initialized with $a(\phi, 0) = 1$ and $v(0) = \pi$, and volume fluctuations are prescribed by Eq. (53) with $\bar{v} = 2$, $\bar{v} = 1$ and $p = 100$. Black and gray colors correspond to $\tilde{n} = 1/2$ and 2, respectively. Solid curves show the path of $\mathbf{x}_c(t)$ and circles mark the positions of the sources/sinks. (b) the evolution of x_c for both cases in (a) with an inset depicting a zoomed-in portion.

where

$$\phi_0 = \tan^{-1} \left(\frac{y_0 - y_c}{x_0 - x_c} \right) \quad \text{and} \quad r_0 = \frac{\sqrt{(x_0 - x_c)^2 + (y_0 - y_c)^2}}{a(\phi_0, t)}, \quad (58b,c)$$

with $r_0 \neq 1$. Eqs. (58) give the location of the mass flux in the (r, ϕ) computational coordinate system so that the injection point remains unchanged in the physical coordinate system. This allows us to evaluate the time-dependent integrals $\zeta_m(t)$ to obtain

$$\zeta_0(t) = -\frac{1}{\pi b_0^2} + \frac{1}{a(\phi_0, t)^2} \frac{r_0^2}{1 - r_0^2}, \quad (59a)$$

$$\zeta_m(t) = \frac{f_m(r_0) e^{-im\phi_0}}{2\pi a(\phi_0, t)^2} - \frac{4b_m(t)}{b_0(t)^3} \int_0^1 f_m(r) (r^{m+1} - r^3) dr, \quad m \geq 1, \quad (59b)$$

so that Eqs. (51) reduce to a system of ordinary differential equations. The integral term in Eq. (59b) can be pre-computed with numerical quadrature, and the value of $f_m(r_0)$ can be determined straightforwardly through spectrally accurate polynomial interpolation.

Like in Part I, we use this δ -flux distribution to achieve directed droplet transport on substrates, by positioning a fluid source or sink sufficiently close to the contact line as a means to push or pull the contact line in the desired direction. We demonstrate this effect for a homogeneous substrate, with fluid injection/extraction occurring over a period p by using Eq. (53), so that in the first/second half of each period mass gain/loss occurs at a different source/sink location. A sample calculation is presented in Fig. 7 where the droplet follows sinusoidal paths by appropriately positioning sources/sinks. Hence, we prescribe the mass flux using

$$q = \dot{v} \delta(x - x_0(t)) \delta(y - y_0(t)), \quad (60)$$

where, during the n -th cycle for which $(n-1)p \leq t < np$, $n \geq 1$, we activate the source/sink locations $(x_0(t), y_0(t))$ according to

$$x_0(t) = \begin{cases} \frac{3}{5} + \frac{n}{5}, & (n-1)p \leq t < (n-1/2)p \quad (\text{source}) \\ -\frac{1}{5} + \frac{n}{5}, & (n-1/2)p \leq t < np \quad (\text{sink}) \end{cases}, \quad y_0(t) = \tilde{n} \sin \left(\frac{x_0(t)}{\tilde{n}} \right), \quad (61)$$

for two cases, namely for $\tilde{n} = 1/2$ and $\tilde{n} = 2$. Initially, the path along which sources/sinks are located is more closely traced by \mathbf{x}_c in the case where $\tilde{n} = 2$ (black curves/symbols). For both cases, the long-time dynamics settle to periodic motion and the paths followed by $\mathbf{x}_c(t)$ prescribe a path that is out of phase from the paths of the corresponding sources/sinks. Additionally, an almost linear evolution in x_c is observed, which becomes indistinguishable as $t \rightarrow \infty$ for both cases considered (see Fig. 7(c)).

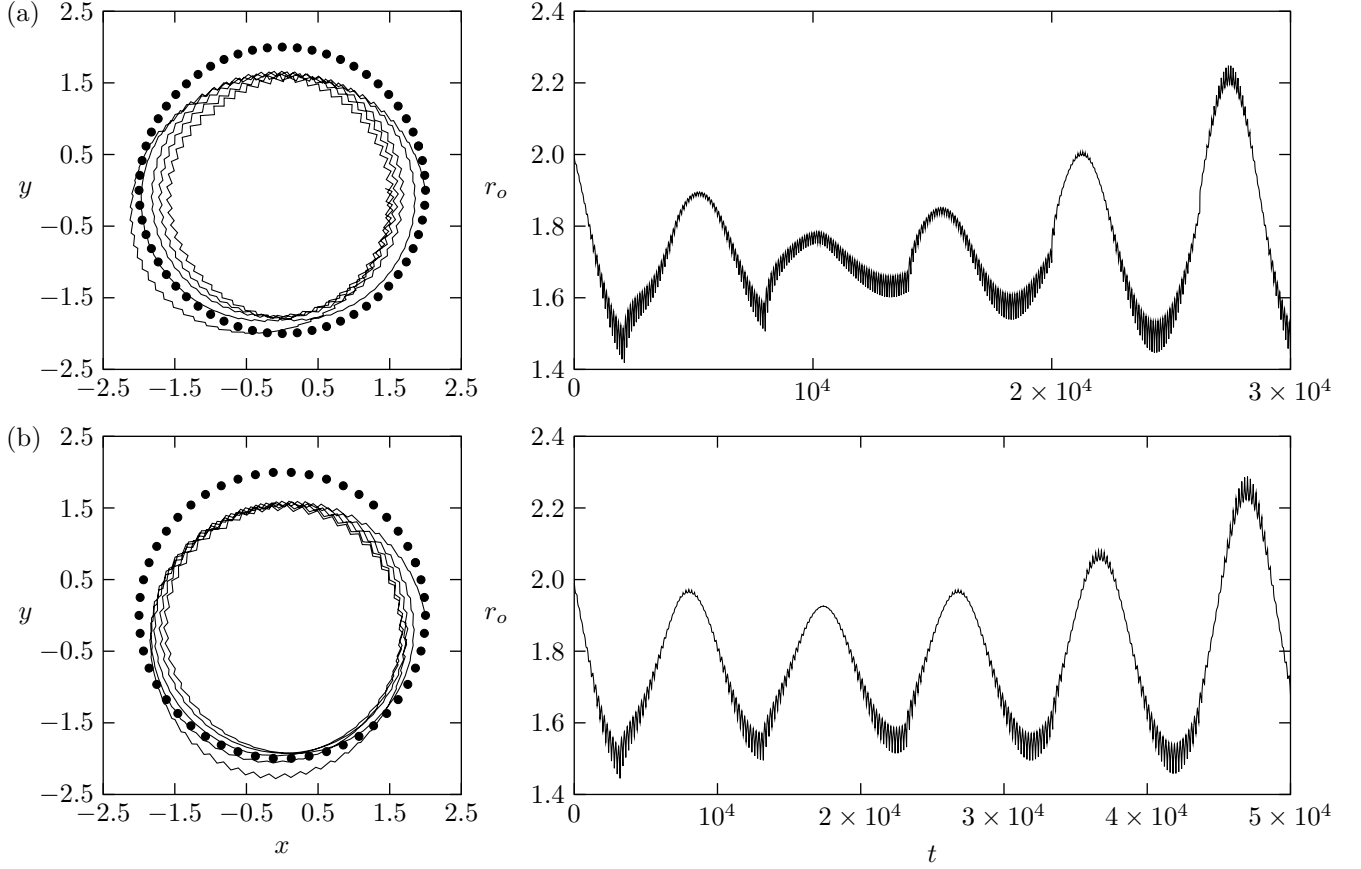


FIG. 8. Droplet transport along nearly circular paths using the reduced model over a homogeneous substrate and q given by Eq. (60), with the sources/sinks activated according to Eq. (62). The droplet is initialised with $a(\phi, 0) = 1$ and $v(0) = \pi$, where volume fluctuations are prescribed by Eq. (53) with $\bar{v} = 2$ and $\tilde{v} = 1$. In panel (a), $p = 100$ and $N = 60$; in panel (b) $p = 200$ and $N = 50$. In each of the panels, the left plots show the path traversed by \mathbf{x}_c (solid curves) together with the sources/sinks (filled circles); the right plots show the evolution of the distance to the origin, $r_o = \sqrt{x_c^2 + y_c^2}$.

Settling to periodic dynamics is not always observed, as shown in Fig. 8. Here, Eq. (60) is used with N equispaced sources and sinks which are positioned along a circular path of radius 2 according to

$$x_0(t) = 2 \cos(\phi_0(t)), \quad (62a)$$

$$y_0(t) = 2 \sin(\phi_0(t)), \quad (62b)$$

where, during the n -th cycle these are activated according to

$$\phi_0(t) = \begin{cases} \frac{2\pi(n+3)}{N}, & (n-1)p \leq t < (n-1/2)p \\ \frac{2\pi(n-1)}{N}, & (n-1/2)p \leq t < np \end{cases}. \quad (62c)$$

Two different cases were considered, namely one with $p = 100$ and $N = 60$ (panel (a) of Fig. 8), and one using $p = 200$ and $N = 50$ (panel (b) of Fig. 8). In both cases, the sources/sinks were activated so that the droplet traveled around the origin five times. As time progressed, sources/sinks were activated closer and closer to the contact line and simulating further in time causes them to be positioned outside the droplet footprint, thus violating the assumptions of our analysis. Likewise, an ill-placed source/sink also arose when using $N = 60$ with $p = 200$ or $N = 50$ with $p = 100$, which suggests that such droplet transport mechanisms must be carefully designed so that the source/sink remains within the droplet footprint for the duration of the motion. Figs. 7 and 8 demonstrate the richness of the system, even for homogeneous substrates. The inclusion of chemical heterogeneities may be leveraged as an additional mechanism to control droplet transport and confinement, e.g. through chemical gradients and wettability barriers.

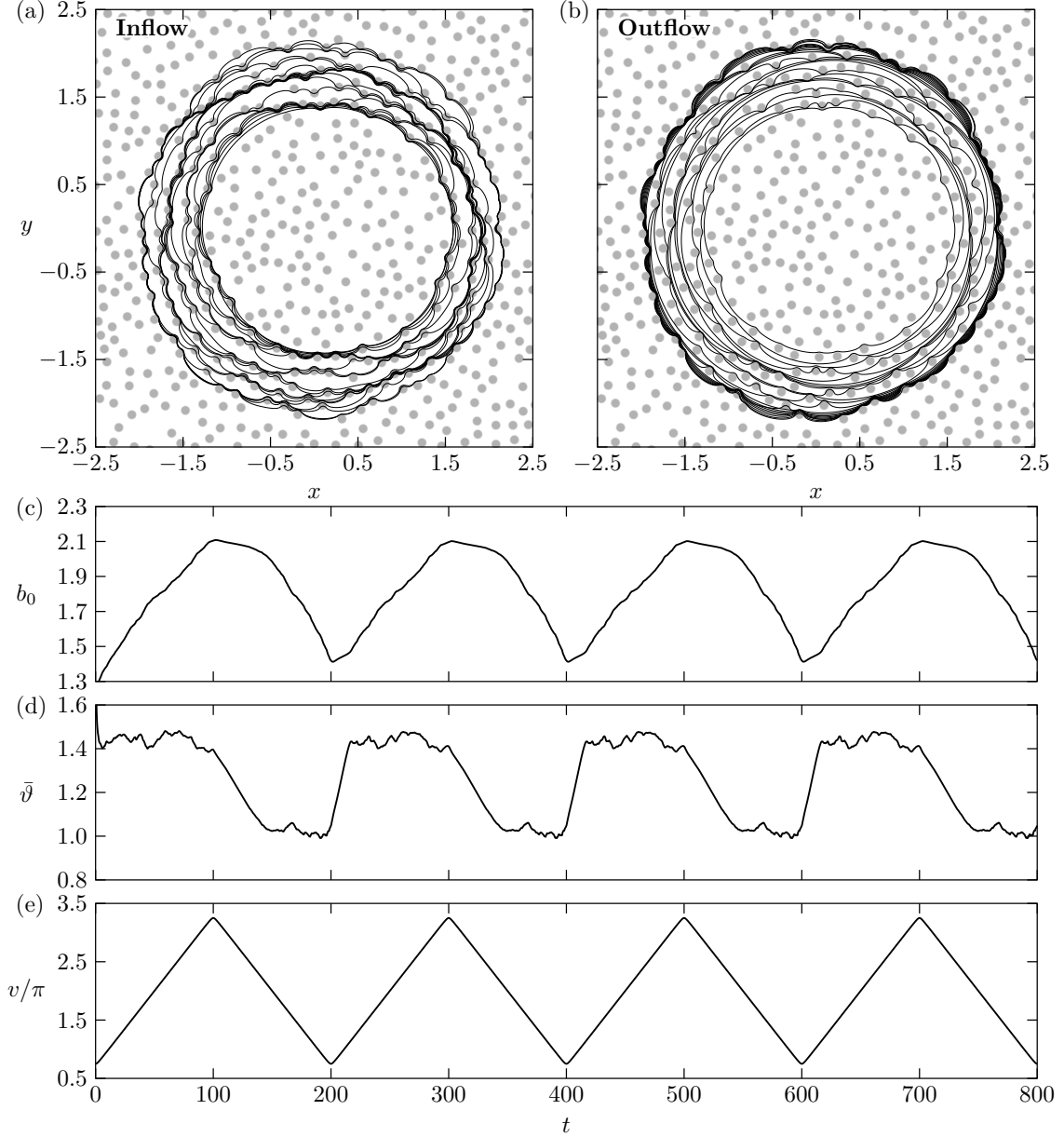


FIG. 9. Volume cycling over a substrate with randomly placed small patches of lower wettability using the reduced model (see text for details on how the substrate is generated). The volume varies according to (53) with parameters $\bar{v} = 2\pi$, $\tilde{v} = 1.25\pi$ and $p = 200$, together with $q(\mathbf{x}, t) = \dot{v}(t)\delta(\mathbf{x})$. (a) Droplet profiles during inflow for $200 \leq t \leq 300$ (b) Droplet profiles during outflow for $300 \leq t \leq 400$. For both cases, profiles are drawn every 5 time units. (c), (d) and (e) show, respectively the evolution of the the mean radius, b_0 , mean apparent contact angle, $\bar{\vartheta}$, and the scaled volume, v/π .

How the volume changes in time also plays an important role, which may enhance or diminish these effects. The influence of these mechanisms on the dynamics arguably deserve a more detailed investigation, which is beyond the scope of the present work.

C. Small-scale features

In this final example we consider a substrate formed with randomly distributed heterogeneous features by using

$$\vartheta(\mathbf{x}) = 1 + \sum_{j=1}^{800} \tilde{\vartheta} \left(\sqrt{(x - \bar{x}_j)^2 + (y - \bar{y}_j)^2} \right), \quad \tilde{\vartheta}(x) = \frac{1}{2} [\tanh(200x + 10) - \tanh(200x - 10)], \quad (63)$$

which prescribes 800 localized circular patches of lower wettability ($\vartheta \approx 2$) with approximate radius 0.05 units and positions (\bar{x}_j, \bar{y}_j) chosen randomly to lie in the square $(-3, 3) \times (-3, 3)$, so that the features are at least 0.15 dimensionless units apart. A similar calculation has been performed in Ref. [12] for the case of constant mass to examine stick-slip behaviours with advancing contact lines. Here, we are interested in the dynamic phenomena that arise from cycling the volume through periodic mass changes. To properly resolve contact line variations occurring at shorter scales would require a very large number of collocation points in the azimuthal direction, which makes solving the full model inefficient with our current implementation and the hybrid model rather challenging due to the solution of large dense matrix-vector equations at each time-step. Hence, we chose to perform this simulation with the reduced model only, although strictly speaking we no longer have $a_0 \gg \partial_\phi a$ as required by the asymptotic analysis undertaken. However, since the reduced model works generally well for other cases considered, we can use it to gather a qualitative outlook on the dynamics that arise and to demonstrate that the model is able to capture the generic features that arise in experimental settings rather well.

The result of the computation is shown in Fig. 9, where dynamically cycling the droplet volume with the localized flux $q(\mathbf{x}, t) = \dot{v}(t)\delta(\mathbf{x})$ gives rise to a number of features present in previous examples. Firstly, it is easy to see from Figs. 9(a) and (b) that pinning/de-pinning events emerge throughout both the inflow and outflow stages. The constant-radius and angle modes also appear as a consequence of the pinning events which suggests, like in Part I, that such behaviours may arise in experimental settings due to substrate features whose effects are more difficult to quantify (see Figs. 9(c) and (d)). Interestingly, the dynamics presented here are qualitatively very similar to Fig. 10 in Ref. [2] by Lam *et al.*, where the authors experimentally analyze cycling the droplet's volume through a needle at its base. Like the results here, Lam *et al.* showed that the constant-radius mode is rather brief and occurs shortly after the flow conditions switch, giving predominately the constant-angle mode. Noteworthy also is that the stick-slip and pinning behaviours are reminiscent of the results in Refs. [27] and [28] by Cubaud and Fermigier, although no direct comparisons can be made because larger droplets are considered where gravitational effects become appreciable, which, in the present case, are neglected in favor of analytical tractability.

V. CONCLUDING REMARKS

The motion of a liquid drop on a solid surface is a process that is rather easy to conceptualise, with numerous applications across science and engineering. However, the underlying physical processes are inherently complex, rendering their study highly non-trivial. Although the long-wave limit yields a single evolution equation for the droplet thickness, its numerical solution becomes considerably challenging as $\lambda \rightarrow 0$. The asymptotic analysis undertaken in this two-part study, is able to mitigate this challenge by developing non-stiff lower-dimensional models for the evolution of the contact line in the 2D and 3D settings.

In this part, we tackled the 3D geometry, building upon the work in Ref. [12] to include the additional terms required to capture droplets of variable mass as prescribed through some spatiotemporal flux function. To simplify the analysis based on the observations of Part I, the assumption that the mass flux vanishes along the contact line was applied so that explicit equations could be obtained for the Fourier coefficients of the contact line, see Eqs. (51). In these equations, like their analogous 2D counterpart (see Eqs. (30), Part I), the contributions of the rate of change of the droplet volume on the contact line shape were accounted for by incorporating time-dependent integral terms involving the mass flux.

To assess the validity of the theory presented here and to explore some interesting physical phenomena associated with droplet spreading, we discussed a number of representative cases that contrasts our theory with simulations to the governing system, Eq. (1). In the majority of the cases considered, we observed excellent agreement between the outcomes of the analysis and the numerical solutions of the full equations, noting that the most optimal agreement is obtained with the hybrid model, particularly in cases when the contact line is more strongly deformed by the heterogeneities.

We examined the balance between liquid flux and chemical heterogeneity, by considering a number of cases motivated by experiments. Let us note that no quantitative comparison with experiments was sought, since, as far as we are aware, no study in the literature reports the time evolution of the contact line, at least within the regime of applicability of our theory. However, we were able to demonstrate that features commonly observed in experimental settings naturally arose through simulations, including stick-slide/stick-jump events and the constant-radius and constant-angle modes. Notably, qualitative comparison between the experimental studies of Dietrich *et al.* who consider evaporating droplets (see Fig. 2) [3], and Lam *et al.* who consider liquid inflow/outflow with a needle (see Fig. 9) [2], were demonstrated. These comparisons were performed with substrates decorated with random heterogeneities. Thus, the observed behaviors emerge due to substrate heterogeneities, whose effects are generally more difficult to assess both in experiments and in full-scale direct numerical simulations. Just like the 2D results, we noted that the dynamics is quite sensitive to the parameters controlling the flux and chemical heterogeneity, showing how small

changes can yield large differences in the subsequent behaviours. Nevertheless, Eqs. (51) were able to predict these behaviours and were in excellent agreement with the solution to the governing equation. This shows that the effort invested in developing the two-term asymptotic expansion of the solution is rewarded with a more favorable agreement compared to solutions obtained using the leading-order equation with little additional computational overhead, see Eq. (55) and Fig. 3.

Throughout this two-part study, the assumption that the mass flux vanishes at the contact line was applied so that changes in mass occurred through the bulk of the droplet. This assumption was not deemed to be restrictive for our purposes, and, indeed, it did not appear to impact the features of the phenomenology we wished to uncover. However, it is inappropriate for investigating mass loss through evaporation, since, in that case, the mass flux is maximized close to the contact line. The asymptotics of such cases, require a specialized treatment of the micro-scale [17, 18], a subject to be explored in more detail in a forthcoming investigation.

VI. ACKNOWLEDGEMENTS

The computations of this work were performed using the computational facilities of the Advanced Research Computing @ Cardiff Division, Cardiff University. DG acknowledges support from the Engineering and Physical Sciences Research Council of the UK through Grant No EP/P505453/1; NS acknowledges support from the European Union's Horizon 2020 research and innovation programme under grant agreement No 810660.

Appendix A: Local expansion of the governing PDE

The equation for the evolution of the two-dimensional contact line $\mathbf{c}(\mathbf{x}, t)$, Eq. (1d), is formally derived by taking a local expansion of the governing PDE

$$\partial_t h + \nabla \cdot [h\mathbf{Q}] = q, \quad (\text{A1})$$

near $\mathbf{x} = \mathbf{c}$, noting that similar considerations were presented in related works (see, e.g. [12, 16, 29]). Here we define $\mathbf{Q} = (h^2 + \lambda^2) \nabla \nabla^2 h$ for notational simplicity, noting that \mathbf{Q} would change should a different slip model be used, or if additional complexities such as substrate topography be included. The leading term of the series expansion near the contact line is

$$h = (\mathbf{x} - \mathbf{c}) \cdot \nabla h|_{\mathbf{x}=\mathbf{c}} + \dots, \quad (\text{A2})$$

where dots denote omitted higher-order corrections, which vanish as $\mathbf{x} \rightarrow \mathbf{c}$. Using this expansion, we can deduce that

$$\partial_t h|_{\mathbf{x}=\mathbf{c}} = -\partial_t \mathbf{c} \cdot \nabla h|_{\mathbf{x}=\mathbf{c}} + \dots, \quad (\text{A3})$$

which, when combined with an expanded form of (A1) about $\mathbf{x} = \mathbf{c}$, yields

$$-\partial_t \mathbf{c} \cdot \nabla h|_{\mathbf{x}=\mathbf{c}} + \mathbf{Q}|_{\mathbf{x}=\mathbf{c}} \cdot \nabla h|_{\mathbf{x}=\mathbf{c}} + \dots = q|_{\mathbf{x}=\mathbf{c}}. \quad (\text{A4})$$

This implies that

$$[(\mathbf{Q} - \partial_t \mathbf{c}) \cdot \nabla h]|_{\mathbf{x}=\mathbf{c}} = q|_{\mathbf{x}=\mathbf{c}}, \quad (\text{A5})$$

which is the corresponding moving boundary condition. This expression can be further simplified using

$$\nabla h|_{\mathbf{x}=\mathbf{c}} = (\nabla h \cdot \boldsymbol{\nu})|_{\mathbf{x}=\mathbf{c}} \boldsymbol{\nu} + (\nabla h \cdot \boldsymbol{\tau})|_{\mathbf{x}=\mathbf{c}} \boldsymbol{\tau}, \quad (\text{A6})$$

where $\boldsymbol{\tau}$ is the unit tangent vector to the contact line (see Fig. 1). Since h does not change along $\boldsymbol{\tau}$ we can write

$$\nabla h|_{\mathbf{x}=\mathbf{c}} = (\nabla h \cdot \boldsymbol{\nu})|_{\mathbf{x}=\mathbf{c}} \boldsymbol{\nu} = -\theta|_{\mathbf{x}=\mathbf{c}} \boldsymbol{\nu}, \quad (\text{A7})$$

giving the final moving boundary condition, Eq. (1d).

[1] H. Y. Erbil, G. McHale, and M. I. Newton, Drop evaporation on solid surfaces: constant contact angle mode, *Langmuir* **18**, 2636 (2002).

- [2] C. Lam, R. Wu, D. Li, M. Hair, and A. Neumann, Study of the advancing and receding contact angles: liquid sorption as a cause of contact angle hysteresis, *Adv. Colloid. Interfac. Sci.* **96**, 169 (2002).
- [3] E. Dietrich, E. S. Kooij, X. Zhang, H. J. W. Zandvliet, and D. Lohse, Stick-jump mode in surface droplet dissolution, *Langmuir* **31**, 4696 (2015).
- [4] J. M. Stauber, S. K. Wilson, B. R. Duffy, and K. Sefiane, Evaporation of droplets on strongly hydrophobic substrates, *Langmuir* **31**, 3653 (2015).
- [5] J. M. Stauber, S. K. Wilson, B. R. Duffy, and K. Sefiane, On the lifetimes of evaporating droplets with related initial and receding contact angles, *Phys. Fluids* **27**, 122101 (2015).
- [6] G. G. Wells, É. Ruiz-Gutiérrez, Y. L. Lirzin, A. Nourry, B. V. Orme, M. Pradas, and R. Ledesma-Aguilar, Snap evaporation of droplets on smooth topographies, *Nat. Commun.* **9**, (2018).
- [7] D. Groves and N. Savva, Droplet motion on chemically heterogeneous substrates with mass transfer. I. Two-dimensional dynamics, <http://arxiv.org/abs/2007.07004>.
- [8] M. Pradas, N. Savva, J. B. Benziger, I. G. Kevrekidis, and S. Kalliadasis, Dynamics of fattening and thinning 2D sessile droplets, *Langmuir* **32**, 4736 (2016).
- [9] S. Afkhami, J. Buongiorno, A. Guion, S. Popinet, Y. Saade, R. Scardovelli, and S. Zaleski, Transition in a numerical model of contact line dynamics and forced dewetting, *J. Comput. Phys.* **374**, 1061 (2018).
- [10] U. Lcís, P. Johansson, T. Fullana, B. Hess, G. Amberg, S. Bagheri, and S. Zaleski, Steady moving contact line of water over a no-slip substrate, <http://arxiv.org/abs/2003.12246v2>.
- [11] Y. Sui, H. Ding, and P. D. M. Spelt, Numerical simulations of flows with moving contact lines, *Ann. Rev. Fluid Mech.* **46**, 97 (2014).
- [12] N. Savva, D. Groves, and S. Kalliadasis, Droplet dynamics on chemically heterogeneous substrates, *J. Fluid Mech.* **859**, 321 (2018).
- [13] H. P. Greenspan, On the motion of a small viscous droplet that wets a surface, *J. Fluid Mech.* **84**, 125 (1978).
- [14] A. A. Lacey, The motion with slip of a thin viscous droplet over a solid surface, *Stud. Appl. Math.* **67**, 217 (1982).
- [15] L. M. Hocking, The spreading of a thin drop by gravity and capillarity, *Q. J. Mech. Appl. Math.* **36**, 55 (1983).
- [16] J. M. Oliver, J. P. Whiteley, M. A. Saxton, D. Vella, V. S. Zubkov, and J. R. King, On contact-line dynamics with mass transfer, *Eur. J. Appl. Math.* **26**, 671 (2015).
- [17] M. A. Saxton, J. P. Whiteley, D. Vella, and J. M. Oliver, On thin evaporating drops: When is the d^2 -law valid?, *J. Fluid Mech.* **792**, 134 (2016).
- [18] N. Savva, A. Rednikov, and P. Colinet, Asymptotic analysis of the evaporation dynamics of partially wetting droplets, *J. Fluid Mech.* **824**, 574 (2017).
- [19] V. S. Ajaev, Spreading of thin volatile liquid droplets on uniformly heated surfaces, *J. Fluid Mech.* **528**, 279 (2005).
- [20] R. Vellingiri, N. Savva, and S. Kalliadasis, Droplet spreading on chemically heterogeneous substrates, *Phys. Rev. E* **84**, (2011).
- [21] D. N. Sibley, A. Nold, and S. Kalliadasis, The asymptotics of the moving contact line: cracking an old nut, *J. Fluid Mech.* **764**, 445 (2015).
- [22] H. Kusumaatmaja and J. M. Yeomans, Controlling drop size and polydispersity using chemically patterned surfaces, *Langmuir* **23**, 956 (2007).
- [23] H.-D. Xi, H. Zheng, W. Guo, A. M. Gañán-Calvo, Y. Ai, C.-W. Tsao, J. Zhou, W. Li, Y. Huang, N.-T. Nguyen, and S. H. Tan, Active droplet sorting in microfluidics: a review, *Lab. Chip* **17**, 751 (2017).
- [24] O. Bliznyuk, E. Vereshchagina, E. S. Kooij, and B. Poelsema, Scaling of anisotropic droplet shapes on chemically stripe-patterned surfaces, *Phys. Rev. E* **79**, (2009).
- [25] R. David and A. W. Neumann, Anisotropic drop shapes on chemically striped surfaces, *Colloids. Surface A* **393**, 32 (2012).
- [26] V. G. Damle and K. Rykaczewski, Nano-striped chemically anisotropic surfaces have near isotropic wettability, *Appl. Phys. Lett.* **110**, 171603 (2017).
- [27] T. Cubaud and M. Fermigier, Advancing contact lines on chemically patterned surfaces, *J. Colloid. Interf. Sci.* **269**, 171 (2004).
- [28] T. Cubaud, M. Fermigier, and P. Jenffer, Spreading of large drops on patterned surfaces, *Oil & Gas Sci. Tech.* **56**, 23 (2001).
- [29] G. W. Young, Mathematical description of viscous free surface flows, in *Free Boundaries in Viscous Flows*, edited by R. A. Brown and S. H. Davis (Springer, 1994) pp. 1–27.